Geophys. J. Int. (2004) **157,** 229–244 doi: 10.1111/j.1365-246X.2004.02170.x

Modelling dynamic stress changes caused by an extended rupture in an elastic stratified half-space

Andrea Antonioli,[1] M. E. Belardinelli[2] and M. Cocco[1]

[1] *Istituto Nazionale di Geofisica e Vulcanologia, Rome, Italy. E-mail: antonioli@ingv.it*
[2] *Università degli Studi di Bologna, Dipartimento di Fisica, Italy*

Accepted 2003 October 15. Received 2003 October 7; in original form 2003 May 16

SUMMARY

We model the time histories of coseismic stress changes produced by an earthquake rupture on an extended fault in a layered elastic half-space. We compute the stress perturbations caused by earthquakes using the discrete wavenumber and the reflectivity methods. We investigate the influence on the computed Coulomb stress changes of the adopted crustal velocity model, the rupture history and slip duration as well as the poro-elastic model assumed to calculate the pore-pressure changes. The comparison between the spatio-temporal evolution of the induced stress field, calculated for different crustal models and rupture histories, allows us to assess the depth and frequency dependence of the induced stress perturbation and the relative weight of dynamic and static stress changes. Our results show that the rise time and the rupture directivity are more important for characterizing the simulated stress time histories than the details of the rupture history. The adopted poro-elastic model affects the static stress changes more than the transient stress perturbations. The results of this study should be taken into account to model fault interaction through elastic stress transfer.

Key words: Coulomb stress, dynamic stress, earthquake rupture, fault interaction.

INTRODUCTION

Fault interaction is currently investigated by stress transfer models at different spatial scales and over different time intervals. Several methodologies have been developed to study the induced stress perturbations caused by coseismic slip on extended faults in the surrounding medium (see Harris 1998; King & Cocco 2000). Coseismic stress changes consist of both transient (dynamic) and permanent (static) components, which decay with distance in a different way (see Cotton & Coutant 1997; Belardinelli *et al.* 1999, and references therein). The role of static and dynamic stress changes in promoting or triggering impending earthquakes is still a matter of discussion and different opinions exist (see Gomberg *et al.* 1998; Harris 1998; Scholz 1998; Gomberg 2001; Antonioli *et al.* 2002; Belardinelli *et al.* 2003, among several others). Kilb *et al.* (2000), Kilb *et al.* (2002) and Gomberg *et al.* (2003) emphasized the role of rupture directivity in focusing dynamic stress perturbations, which can affect the spatial aftershock pattern. Static stress changes are usually calculated by solving the elastostatic equation in an elastic, homogeneous half-space (Okada 1985, 1992) and they are applied to model aftershock patterns, seismicity rate changes and interactions between large magnitude earthquakes (see Harris 1998; Stein 1999; King & Cocco 2000). Furthermore, static and dynamic stress changes can be computed by solving the elastodynamic equation in a layered (1-D) half-space (Cotton & Coutant 1997).

Despite all of these studies and applications to different areas, a detailed and systematic investigation of the effects of the crustal structure and rupture history on the induced coseismic (transient and permanent) stress changes has never been published. The goal of this paper is to present a systematic comparison between the stress time histories calculated for different crustal velocity and source models. We aim to understand the depth dependence and the attenuation of the dynamic and static stress amplitudes. This represents, in our opinion, the basic information required to discuss and interpret the spatial variability of stress perturbations and the relative effects of dynamic and static stress changes. The determination of the triggering delay (i.e. the time difference between the occurrence of an induced failure and the time of application of the induced load) caused by the stress perturbation depends on the arrival times of the positive stress peaks and of the amplitude and frequency content of the transient stress time history (see Belardinelli *et al.* 2003, and references therein). All of these quantities are affected by the crustal structure and the rupture history on the causative fault. Moreover, the comparison between Coulomb stress changes and the aftershock distribution is made by mapping the induced stress perturbations at fixed depths. Thus, the depth dependence of these stress changes is crucial in order to evaluate event correlations quantitatively. These represent only some of the motivations for the present study.

We calculate the time histories of coseismic stress changes using a discrete wavenumber and reflectivity method (see Cotton & Coutant 1997). We compute stress changes caused by a kinematic

rupture model in a layered elastic half-space. We perform our numerical calculations of Coulomb stress changes using two different poro-elastic models to account for the pore pressure changes. We compare the stress changes resulting from a constant apparent friction model and an isotropic poro-elastic model (see Beeler *et al.* 2000, and references therein). Recently, Cocco & Rice (2002) have shown that the adoption of a constant apparent friction model can be valid only for a few specific cases, while an isotropic poro-elastic model is in general applicable to an elastic half-space. Both Beeler *et al.* (2000) and Cocco & Rice (2002) have shown that these two poro-elastic models yield very different static Coulomb stress perturbations. In this study, we extend this comparison to transient stress changes.

METHODOLOGY

We compute the stress tensor induced by earthquake ruptures using the reflectivity method (Kennet & Kerry 1979) and the discrete wavenumber decomposition of the Green functions (Bouchon 1981). This method, developed by Cotton & Coutant (1997), allows us to study the temporal stress dependence in an axisymmetric stratified medium. The stress changes are generated by an extended shear rupture embedded in a layered half-space. We discretize the rupturing fault by means of a set of subfaults (point sources) on which we specify the source time function, the slip and the rupture times (i.e. the rupture front propagation). The subfaults are uniformly distributed on the extended fault plane. Each subfault is characterized by the assigned values of strike, dip, rake slip amplitudes and rupture time.

We find the radiated displacement by means of the convolution with the Green functions computed in a layered half-space characterized by the density, *P*- and *S*-wave velocities and, eventually, the anelastic attenuation parameters (Q_p and Q_s). The six components of the stress evolution $\sigma_{ij}(\mathbf{y}, t)$ are obtained by analytically differentiating the ground displacement with respect to the spatial coordinates, which is done in the frequency domain using a Fourier transform. Cotton & Coutant (1997) and Belardinelli *et al.* (1999) give a detailed description of the method. With respect to most of the elastostatic solutions, which are calculated in a homogeneous half-space, the proposed model is suitable for studying the effect of the stratification and the rupture history of the Earth.

We aim to analyse the temporal dependence of the Coulomb stress changes represented by the Coulomb failure function (CFF); toward this goal we compute the shear and the normal stress changes ($\Delta\tau(\mathbf{y}, t)$ and $\Delta\sigma_n(\mathbf{y}, t)$, respectively; the latter is positive for extension) on a specified secondary fault plane (or an array of receivers). According to the definition of CFF (see Harris 1998, and references therein) the Coulomb stress changes are

$$\Delta\mathrm{CFF}(\mathbf{y}, t) = \Delta\tau(\mathbf{y}, t) + \mu[\Delta\sigma_n(\mathbf{y}, t) + \Delta P(\mathbf{y}, t)], \quad (1)$$

where μ is the friction coefficient and ΔP is the induced pressure changes. According to the apparent constant friction model (see Beeler *et al.* 2000, and references therein), the coseismic pore pressure change are assumed to be proportional to the normal stress changes

$$\Delta P = -B\Delta\sigma_n, \quad (2)$$

where B for rock is similar to the Skempton coefficient (Rice & Cleary 1976). This yields the common expression for the Coulomb stress change:

$$\Delta\mathrm{CFF}(\mathbf{y}, t) = \Delta\tau(\mathbf{y}, t) + \mu'\Delta\sigma_n(\mathbf{y}, t), \quad (3)$$

where μ' is the apparent friction coefficient ($\mu' = \mu(1 - B)$; Harris & Simpson 1992; Cocco & Rice 2002). In this study we assume that μ' is 0.4, as widely adopted in the literature (King *et al.* 1994; Nostro *et al.* 1997). Unless specified otherwise, in the following sections we use the apparent friction model (3). In order to image the induced stress field in the regions surrounding the causative fault, we calculate the Coulomb stress changes (ΔCFF) on a set of receiver points. At each receiver point we specify the strike, dip and rake angles that characterize the expected motion of a secondary fault located there. In our calculations, we have to specify the maximum frequency, which strongly affects the computational times. For most of the applications presented in this study, we compute the stress components up to a maximum frequency of 2.26 Hz, unless specified otherwise. It is important to remark that the computed stress time history is band-limited at high frequencies.

DYNAMIC STRESS CHANGES IN A LAYERED MEDIUM: THE EFFECT OF THE CRUSTAL STRUCTURE

In order to investigate the coseismic stress changes caused by an earthquake rupture in a layered medium, we simulate the stress redistributed by the 1980 Irpinia (southern Italy) normal faulting earthquake, for which reliable information exists on the source model and the crustal structure (e.g. Cocco & Pacor 1993; Giardini 1993). This event consists of three distinct subevents that ruptured within 40 s on two antithetic normal faults oriented along the Apennines. Fig. 1 shows the fault geometry, the fault plane solutions for each subevent, the moment rate function and the aftershock distribution. The first fault is fragmented into two segments that ruptured 20 s from each other. Nostro *et al.* (1997) computed the static stress changes caused by the Irpinia event to model fault interaction and the aftershock pattern. Belardinelli *et al.* (1999) modelled both the dynamic and the static stress changes caused by the first subevent on the fault plane of the second. The main subevent (0 s subevent) occurred on a normal fault (rake 270°) dipping 60° NE and striking N315°. The seismic moment for this subevent is 1.7×10^{19} N m, while the total seismic moment for the whole earthquake is 2.6×10^{19} N m (Giardini 1993). The master 0 s fault is 36 km long, with a width of 16 km. We discretized the master fault with 144 square subfaults with a length of 2.0 km. This parametrization was thoroughly tested by Belardinelli *et al.* (1999) and it is suitable for modelling stress changes at distances greater than a few kilometres from the master fault. The source time function is a Bouchon ramp function [$f(t) = 1/2(1 + \tanh(t/\tau)$, Bouchon 1981] with an assigned rise time, τ. As a result of our lack of knowledge concerning the real duration of the slip, in the simulations presented in this study we use rise times ranging between of 1.0 and 3.0 s. We assume for these simulations a homogeneous slip distribution on the main fault with a slip amplitude of 1.16 m; the rupture nucleates at 11 km from the southern edge of the 0 s fault and at 8.6 km depth. The rupture time distribution is taken from Cocco & Pacor (1993), who imaged the rupture history by inverting strong motion waveforms.

In our simulations, we use two different velocity models (Table 1), a homogeneous half-space and a non-Poissonian layered half-space. We compute the shear and the normal stress changes projecting the components of the induced stress tensor (σ_{ij}) on the fault plane of the second subevent of the Irpinia earthquake (the 20 s fault), which has the same dip and rake as the main subevent but a slightly rotated strike N305° (Pantosti & Valensise 1990; Nostro *et al.* 1997). Belardinelli *et al.* (1999) performed a similar test, but they limited

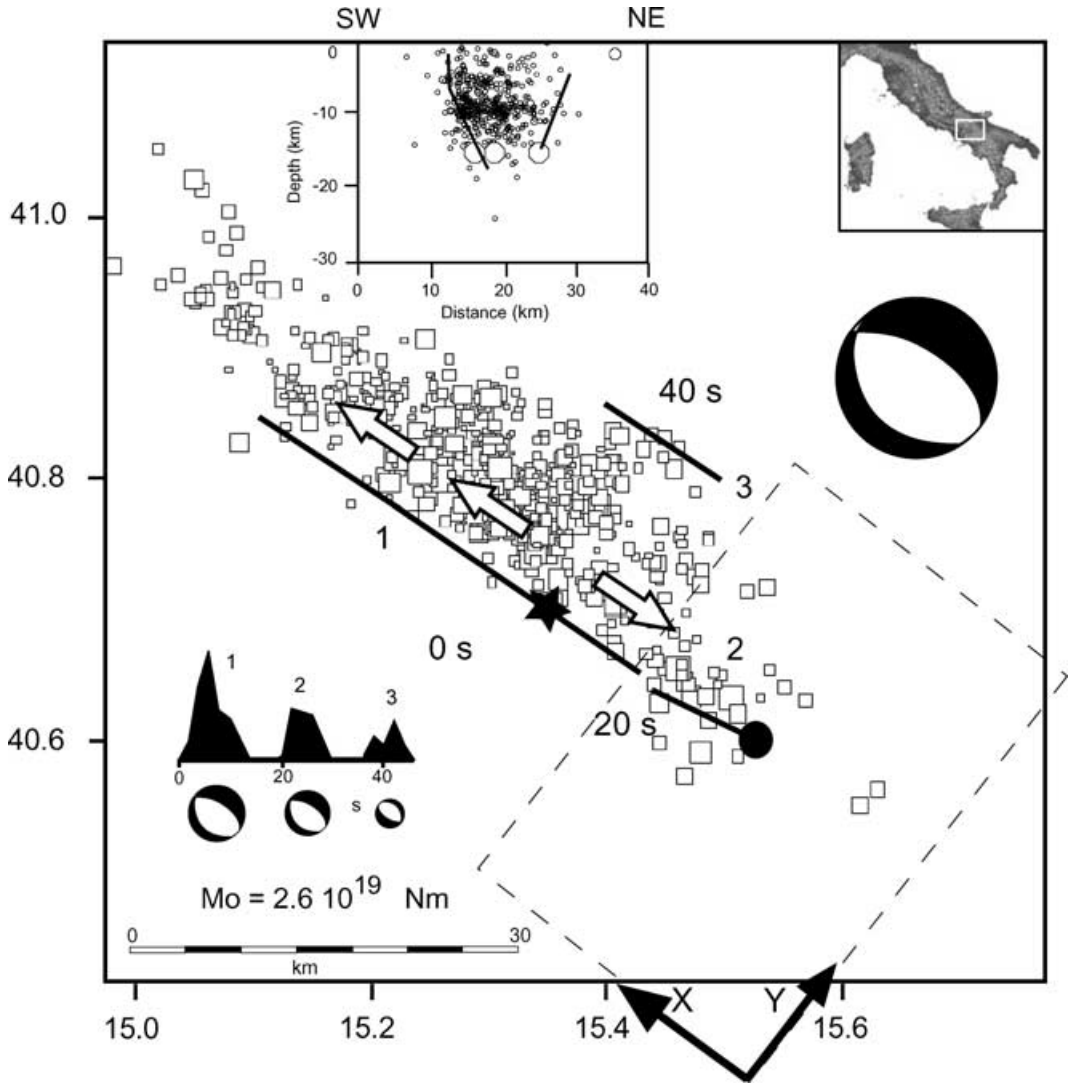

Figure 1. Fault geometry, aftershock distribution, focal mechanism and source time functions of the 1980 Irpinia earthquake (from Belardinelli *et al.* 1999). The aftershock distribution in a cross-section perpendicular to fault 1 is shown. The dark star is the epicentre. The X direction is oriented along the strike of fault 1. The dynamic stress map computations are performed in the dashed box in Fig. 2 and the solid circle is the projection of the vertical profile along which we compute the profiles shown in Figs 3 and 4.

Table 1. Crustal structure.

v_p (km s^{-1})	v_s (km s^{-1})	ρ (Mg m^{-3})	d (km)
	Heterogeneous half-space		
2.65	1.53	2.60	3.0
4.80	2.50	2.60	6.0
5.20	2.65	2.60	10.0
6.30	3.50	2.60	25.0
7.50	4.33	2.60	...
	Homogeneous half-space		
5.00	2.90	2.60	...

their analysis to a single receiver. They emphasized the attenuation of both stress peaks and the static stress level when a heterogeneous crustal model, characterized by shallow low-velocity layers, is adopted. Moreover, they showed that in the layered half-space, the absolute arrival time of the dynamic stress peaks is only slightly delayed compared with the arrival time for the homogeneous one. In this study we present a more through and general test. We perform different calculations either in a horizontal array configuration of receivers or along a vertical profile to test the dependence of the transient stress changes on the structure of the medium (see Fig. 1). We plot the dynamic stress changes at a fixed depth on a map view (shown by a box in Fig. 1) that includes the southern edge of the 0 s fault and the whole 20 s fault. For these simulations, we use 45 receivers with a spatial step of 5 km along the x-axis and 7 km along the y-axis.

indentFor the homogenous velocity model, we show in Fig. 2(a) snapshots of the Coulomb stress changes at different times on a map-view at 8 km depth. For these calculations we use a simple rupture history consisting of a Haskell rupture front and a Bouchon source time function with a rise time of 1.4 s. These results are in agreement with those obtained by Belardinelli *et al.* (1999, see Plate 3 in that paper): the Coulomb stress concentration is located in front of the rupture edge of the first subevent where the 20 s rupture probably nucleated. The stress peak is reached after 6–7 s. Fig. 2(b) shows similar calculations but for the layered model described in Table 1.

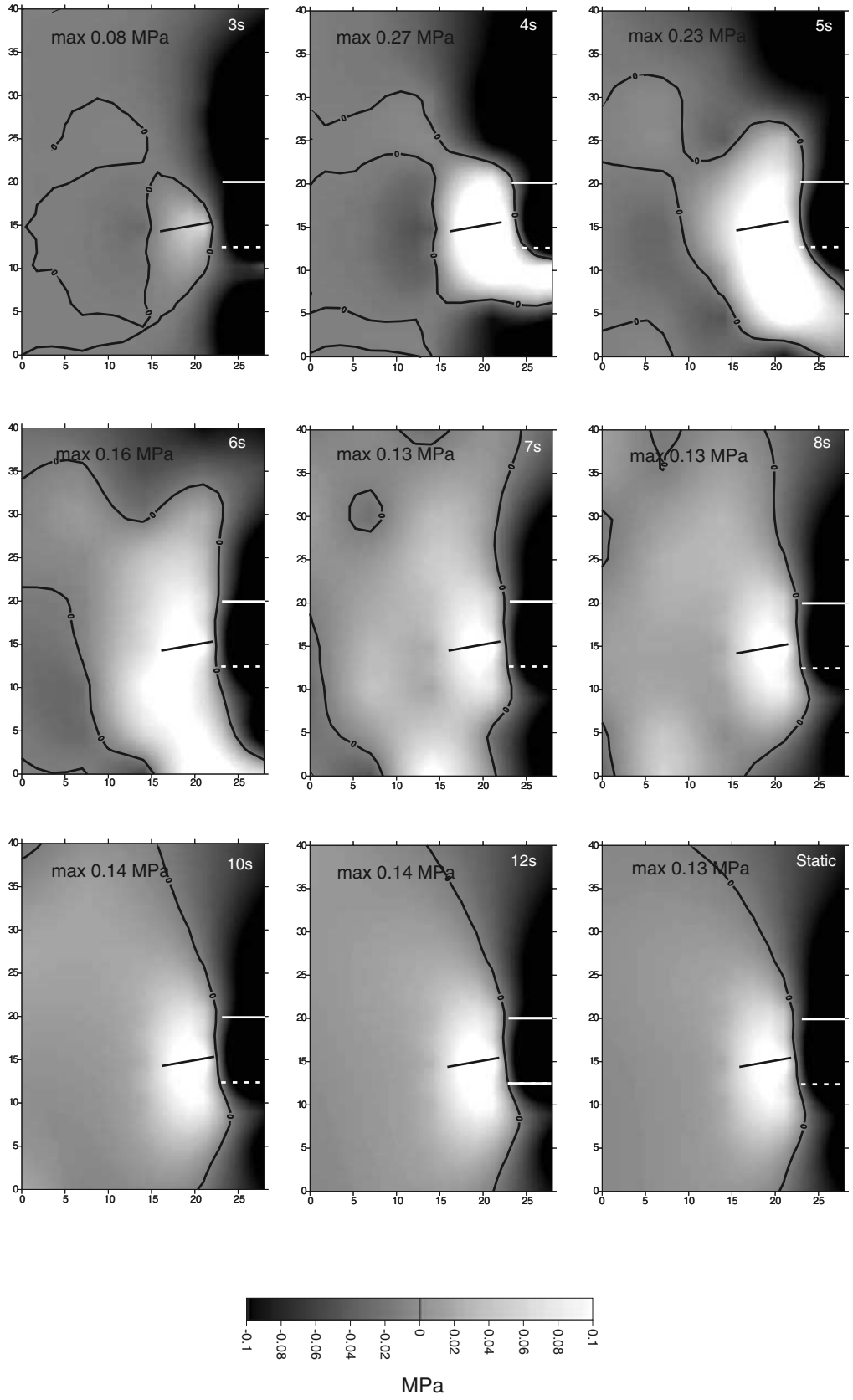

Figure 2. Map view of the Coulomb stress projected on the 20 s fault plane, generated by the Irpinia 1980 earthquake projected at 8 km depth at different times from the 0 s subevent (indicated in the top right-hand corner). The dashed box in Fig. 1 depicts the region mapped in this figure. The 0 s fault trace is indicated by the continuous white line, while its depth position is the dotted white line. The dark line shows the position of the 20 s fault at 8 km depth. The thin dark lines show the 0 MPa contours. In Fig. 2(a) the Coulomb stress changes are computed in a homogeneous half-space, in Fig. 2(b) a layered half-space is used.

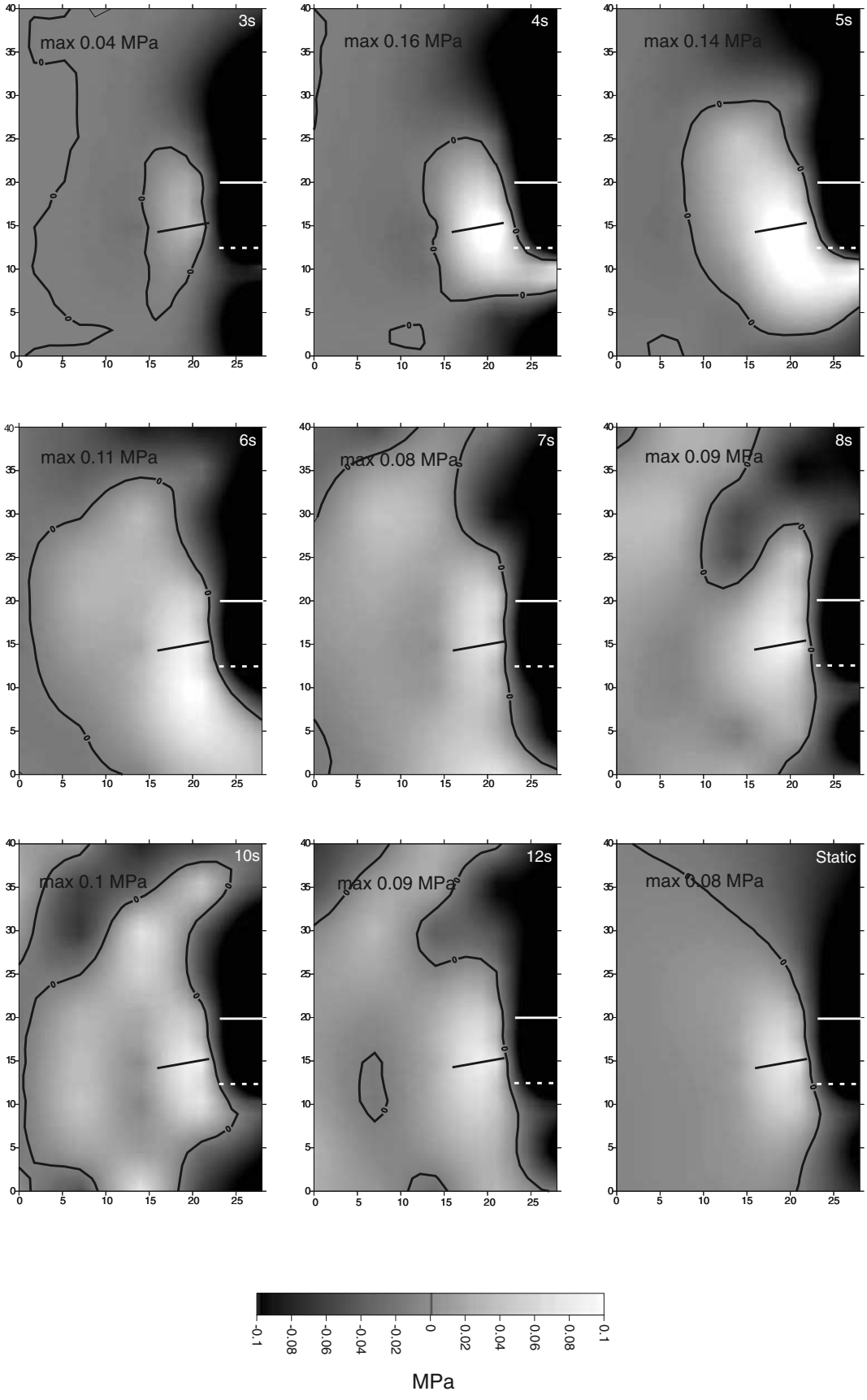

Figure 2. (*Continued.*)

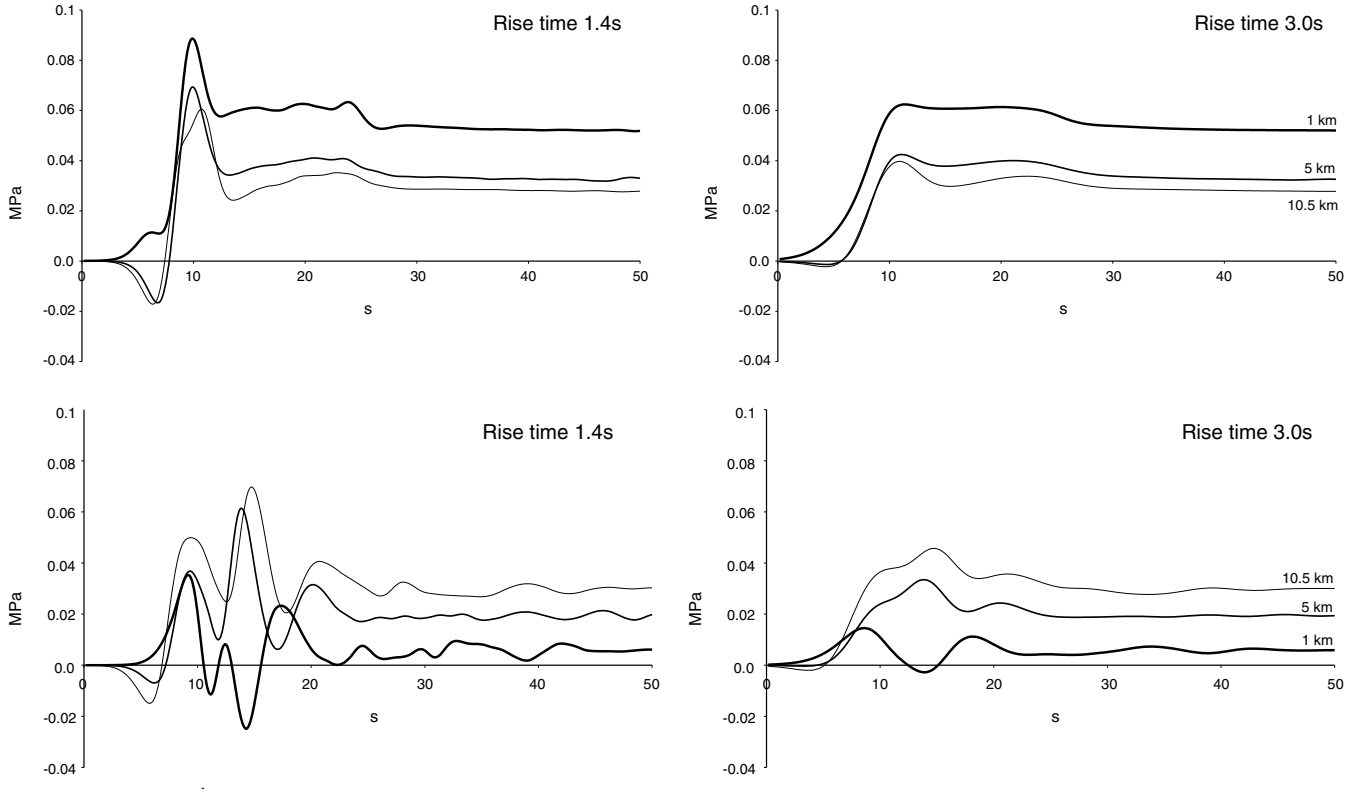

Figure 3. Dynamic Coulomb stress changes generated by the Irpinia 1980 earthquake projected on the 20 s fault plane, and computed along a vertical profile. The projection of receivers on the surface is shown by the solid dot in Fig. 1. The receiver depths are shown in the figures. In Fig. 3(a) we used the homogeneous model and in Fig. 3(b) the layered one. The adopted rise time is indicated in each plot.

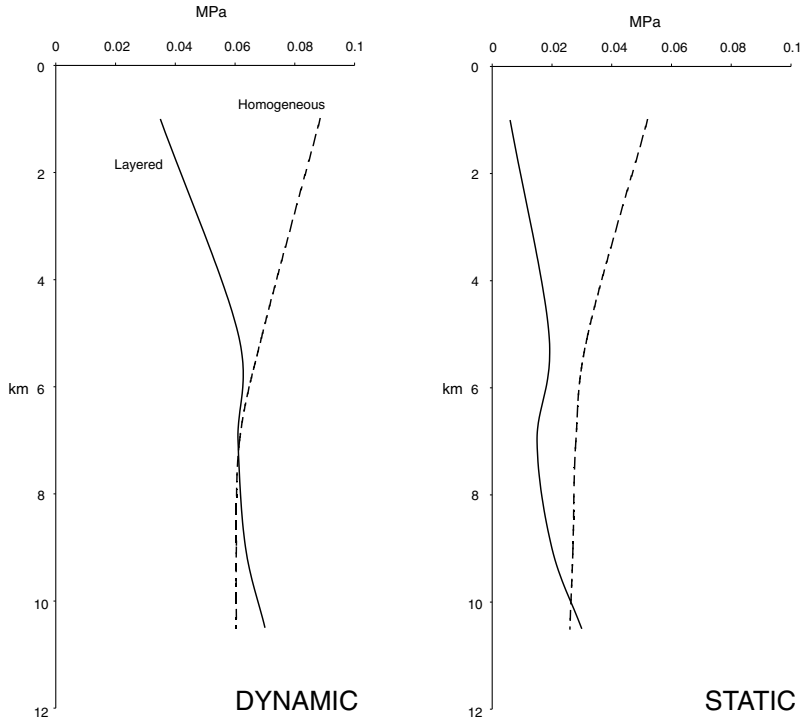

Figure 4. Dynamic and static Coulomb stress amplitudes as a function of depth for the Irpinia 1980 earthquake and for the two velocity models considered here (Table 1). The dynamic stress value refers to the highest stress peak. The receivers are placed along the vertical profile indicated by the solid dot in Fig. 1. We used a 1.4 s rise time.

Fig. 2 shows that the layered crustal model yields a more heterogeneous stress pattern during the transient stress evolution, as is evident from the comparison between the maps at the same instant of time. The static stress increase along the strike direction of the 20 s fault is larger for the homogeneous model. However, the final spatial patterns of static stress perturbations, reached after 25 s, are similar.

We also computed the Coulomb stress changes on receivers placed at different depths along the dip direction of the 20 s fault at the southeastern edge of that plane (the position of the shallowest receiver is shown by the solid dot in Fig. 1). These receivers are located in such a way that the Coulomb stress changes are dominated by the shear stress component, while the contribution from the normal stress component is negligible (Nostro *et al.* 1997). The Coulomb stress time histories are shown in Fig. 3, both for the homogeneous half-space (a) and for the layered crustal model (b). For each of these velocity models we used two different rise times: 1.4 and 3.0 s. The stress time histories calculated for the homogeneous medium (Fig. 3a) are much smoother than those computed for the layered structure (Fig. 3b) and they show a faster approach to the static stress level. We note in Fig. 3 that the frequency content of the stress time histories depends on both the adopted crustal model and the rise time. As expected, this figure shows that the final (permanent) static stress amplitudes do not depend on the adopted rise time but only on the velocity structure. Shallow and deep receivers have similar stress time histories for the homogeneous half-space; the same is not true for the layered velocity model. The stress time histories reveal a stronger dependence on the receiver depth for a layered crustal model. Increasing the rise time results in a low-pass filtering of the radiated seismic waves; consequently the stress time histories have less high-frequency content, as is evident in Fig. 3. The presence of a layered structure produces a more complex propagation path (with multiple reflections and refractions) that generates complex time histories with high-frequency positive and negative stress peaks.

Fig. 4 shows the depth dependence of the stress amplitudes for dynamic and static perturbations for the layered and the homogeneous models. The dynamic stress value refers to the highest stress peak. This figure reveals a different trend with depth of the stress amplitudes for the two crustal models. For this specific configuration, both the dynamic and the static stress amplitudes increase on average with depth in the layered model, while they decrease for the homogeneous half-space. The receiver placed in the upper low-velocity layer at less than 4 km depth in Fig. 4 shows the smallest dynamic and static amplitudes in the layered model. This effect is more pronounced for dynamic stress changes. At a depth larger than 7 km, our simulations predict higher dynamic stress amplitudes in the layered model than in the homogeneous one. Although the depth dependence discussed here is certainly affected by our choice of velocity models, our results highlight the importance of

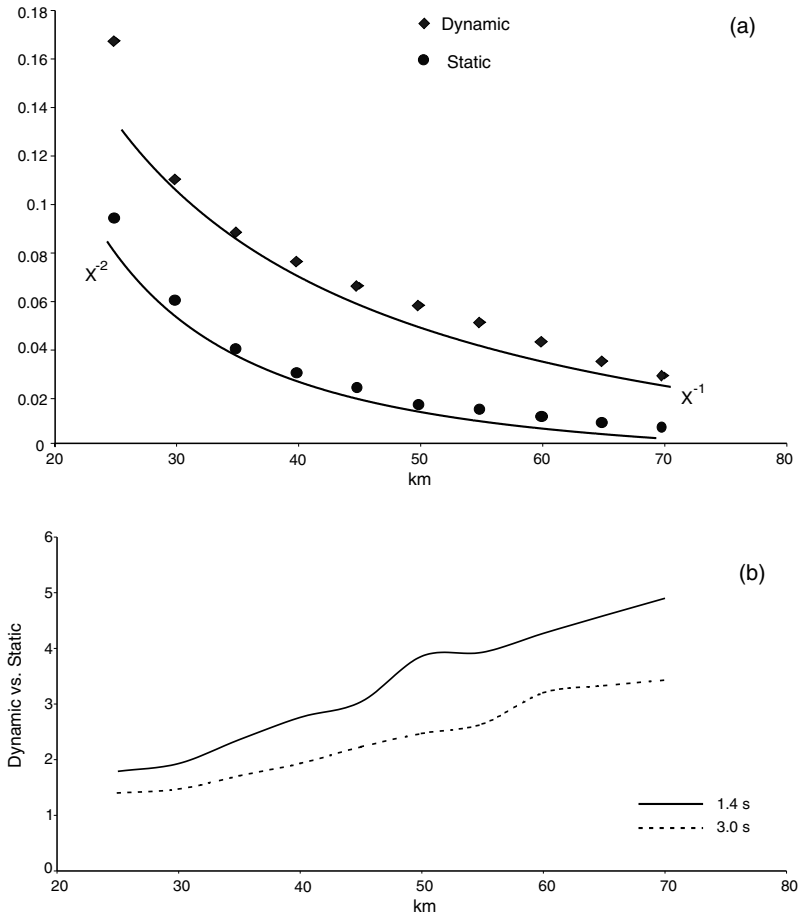

Figure 5. (a) Dynamic (diamonds) and static (circles) Coulomb stress values as a function of the distance along a direction perpendicular (x direction) to the Irpinia master fault strike (0 s) at 8 km depth, in the stratified half-space. The thin dark lines show an analytical decay rate of the two components (x^{-1} for dynamic stress and x^{-2} for static stress). (b) Ratio of dynamic and static Coulomb failure functions. The solid line refers to a rise time of 1.4 s and the dotted line to a rise time of 3.0 s.

using a realistic medium structure. The dynamic stress changes at depths shallower than 6 km for these particular crustal models differ by up to 50 per cent. Even larger relative differences are evident for static stress changes in the whole depth range considered in Fig. 4.

In order to discuss the different geometrical attenuation of transient and permanent stress amplitudes, we show in Fig. 5 the dynamic and static stress amplitudes and their ratio as a function of the distance along a horizontal direction perpendicular to the master fault strike and intersecting the strike direction at the middle point of the fault trace. The computation is performed in the stratified half-space. Fig. 5(a) shows that the amplitudes of static stress changes decay with distance faster than the dynamic stress peaks. The dynamic stress decay is nearly proportional to x^{-1}, while the static amplitudes show a stronger attenuation (proportional to x^{-2}), in agreement with Cotton & Coutant (1997). In Fig. 5(b) we show the ratio between dynamic and static amplitudes resulting from the calculations performed with two different rise times (1.4 and 3.0 s). This figure confirms the stronger attenuation of static stress amplitudes: for instance at 70 km from the master fault, dynamic amplitudes computed for a rise time of 3.0 s are more than twice as great as the static ones. This difference becomes four times for a rise time of 1.4 s. This means that the dynamic stress peak is strongly affected by the adopted source time function and its duration. In the following sections, we will also show the amplitude attenuation along the fault strike direction.

THE EFFECTS OF THE RUPTURE HISTORY ON DYNAMIC STRESS CHANGES

In this section, we aim to discuss the effects of the rupture history on the calculated time evolution of the stress perturbations. We use a different fault geometry and faulting mechanism compared with the previous simulations: we model the stress changes caused by a left-lateral strike-slip fault (rake 180°) 30 km long and 14 km wide, dipping 110° in the homogeneous half-space of Table 1 (see Fig. 6). We discretized the fault with 105 square subsources characterized by their strike, dip, rake, slip and rupture time values (a 15 × 7 lattice of point sources distributed uniformly on the rupture plane). We assume that the rupture nucleates close to the fault edge (open star in Fig. 6), and it is nearly unilateral. In order to emphasize the high frequencies, we adopted a 1.4 s rise time. We compare the stress time histories resulting from a simple Haskell model, characterized by a constant rupture velocity equal to 2.6 km s^{-1}, a constant slip distribution of 1 m and a heterogeneous (more realistic) rupture front propagation model (Fig. 6). The receiver locations are shown at the bottom of the figure (dark stars); they are located at 7 km depth. These simulations are carried out to evaluate if the complexities of the rupture front are of relevance for the computation of the coseismic stress perturbations.

In Fig. 7(a) we compare the Coulomb stress changes caused by these two rupture models for the three receivers shown by the dark stars in Fig. 6. The Coulomb stress changes are calculated for a secondary fault having the same parameters as the master fault. Noticeably, the effect of rupture history is not so relevant: it just modifies the amplitudes of the local minima and maxima of the stress as a function of time. This effect is more pronounced for the directive receiver (number 1 in Fig. 7a). The timing of the stress peaks is slightly modified with the changing rupture history. Fig. 7(b) shows time histories of the shear, normal and associated

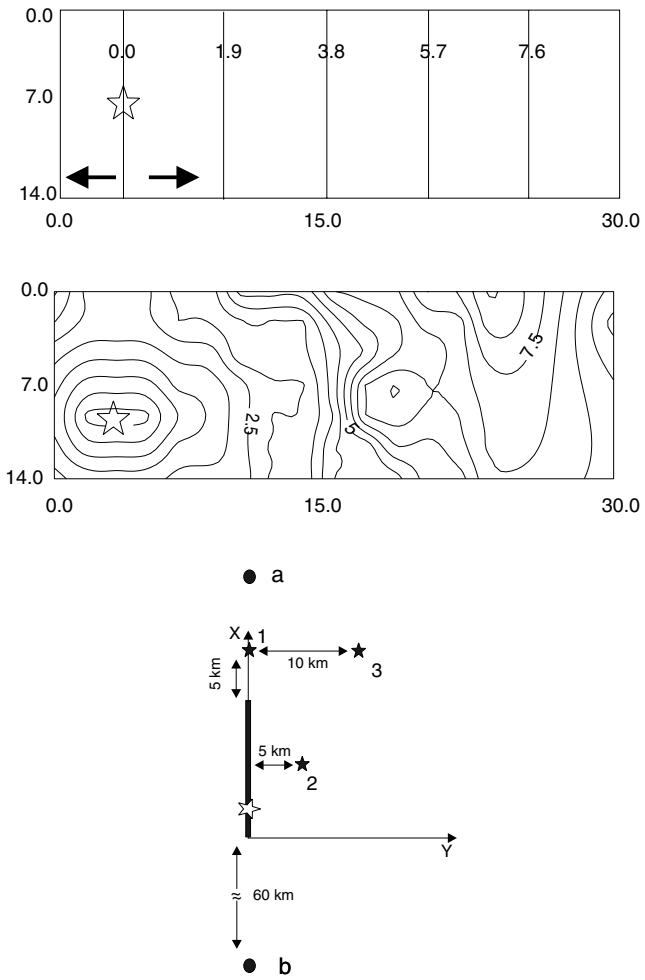

Figure 6. Rupture history employed in the calculation of the effects of the dynamic rupture on the stress diffusion. Top: adopted Haskell-like rupture and real rupture. The white star is the start of the rupture and the thin lines are isochrones. Bottom: map view of the receiver points with respect to the fault trace (thick line). Dark stars (depth 7 km) are the receivers considered in Fig. 7 and dots (depth 0 km) represent the receivers considered in Figs 8 and 9.

CFF perturbation caused by the heterogeneous rupture model shown in Fig. 6. This figure shows that the static CFF changes are mostly due to the shear component. The normal stress changes are relevant in the transient stage.

The heterogeneous rupture front propagation slightly modifies the frequency content of the simulated stress time histories. This is evident in Fig. 8, where we compare the time-series and the Fourier spectra of the stress time histories using the two different rupture model of Fig. 6. We show the stress time histories (stressgrams) either computed for a directive receiver (located in front of the rupture propagation direction, named *a* in Fig. 6) or for a receiver located backward from the rupture propagation (*b* in Fig. 6). The two rupture models produce different transient stress perturbations only for directive receivers.

These simulations suggest that the effect of the heterogeneous rupture front propagation does not modify substantially the calculated stress time histories unless the receiver is affected by directivity effects. According to our results, the rupture directivity is more important in characterizing the dynamic stress changes than the details of the rupture history are as we will see in the following

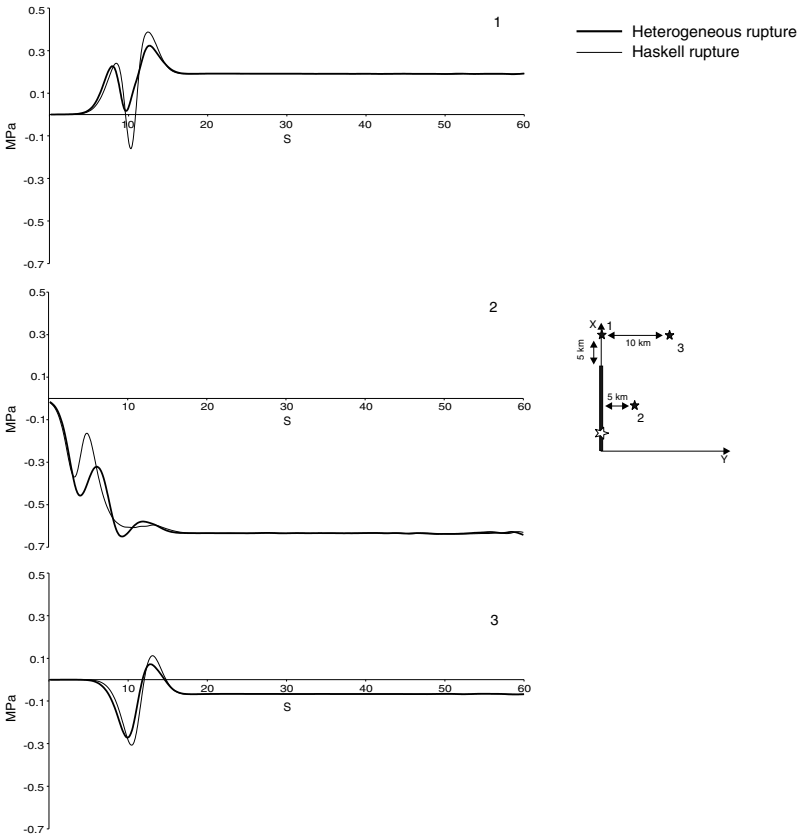

Figure 7. (a) CFF as a function of time at the three different points indicated by the dark stars in Fig. 6 at 7 km depth in the homogeneous model. The thin line represent the dynamic Coulomb failure function generated by a left lateral fault with a Haskell-like rupture (see the text for details), while the thick line displays the CFF of the heterogeneous rupture shown in Fig. 6. (b) Computation of the components of the dynamic Coulomb failure function normal and shear stress as a function of time in the case of the heterogeneous rupture evaluated at the three points indicated by the dark stars of Fig. 6.

section. We have to remark, however, that this conclusion is valid for smooth source time functions and low-frequency Green's functions.

THE EFFECT OF RUPTURE DIRECTIVITY

In this section, we discuss the results of several simulations that illustrate the effect of rupture directivity on the calculated transient (dynamic) stress changes. First we compare the waveforms of synthetic ground velocity with the stress time histories calculated at the Earth's surface for the Haskell source model and homogeneous velocity structure described above and shown in Fig. 6. Synthetic seismograms have been computed with the discrete wavenumber finite-element code proposed by Spudich & Frazer (1984). The fault parametrization adopted in the two numerical approaches is the same. Synthetic ground velocities are low-pass filtered at 2 Hz, in order to compare them with the dynamic stress history. The stress and ground velocity waveforms are calculated at two surface receivers is in front of and behind the rupture at a distance of 60 km from the fault edges (locations a and b in Fig. 6). The three components of the ground velocity and the three non-zero components of the stress perturbation (the other three vanish because we perform our calculations at the free surface) are shown in Fig. 9. This figure emphasizes that directivity effects control the stress change amplitudes and the frequency content similarly to what is commonly observed for real seismograms. In fact, the stress components in the receiver (*a*) have peaks separated by shorter time intervals than those in the receiver (*b*). Moreover, Fig. 9 shows that, for the configuration considered here, relevant dynamic stress changes are associated with the body wave arrivals.

In order to quantify the directivity effect on the transient stress perturbation we plot in Fig. 10 the Coulomb stress time histories calculated for an array of receivers located at different distances from fault edges in the two opposite directions along the fault strike (see the sketch on the left-hand side of the figure). The rupture history is again a simple Haskell rupture model and the medium is homogeneous, as in the previous calculations. For each receiver pair (defined by those symmetrically located along the strike direction at the same distance from each fault edge), rupture directivity generates larger amplitude dynamic stresses in the directive site than in the other one. Fig. 10(b) shows that this effect persists at large distances. These results are summarized in Fig. 11, which shows the amplitude decay of Coulomb stress changes with the distance from the fault. The trend of the amplitude decay is the same, but the amplitudes for the directive receivers are much larger. This is consistent with the findings of Kilb *et al.* (2000, 2002), who proposed an asymmetric pattern of dynamic stress changes caused by the rupture directivity.

Our results illustrate that rupture directivity affects the time histories of Coulomb stress changes, and that this effect is more important

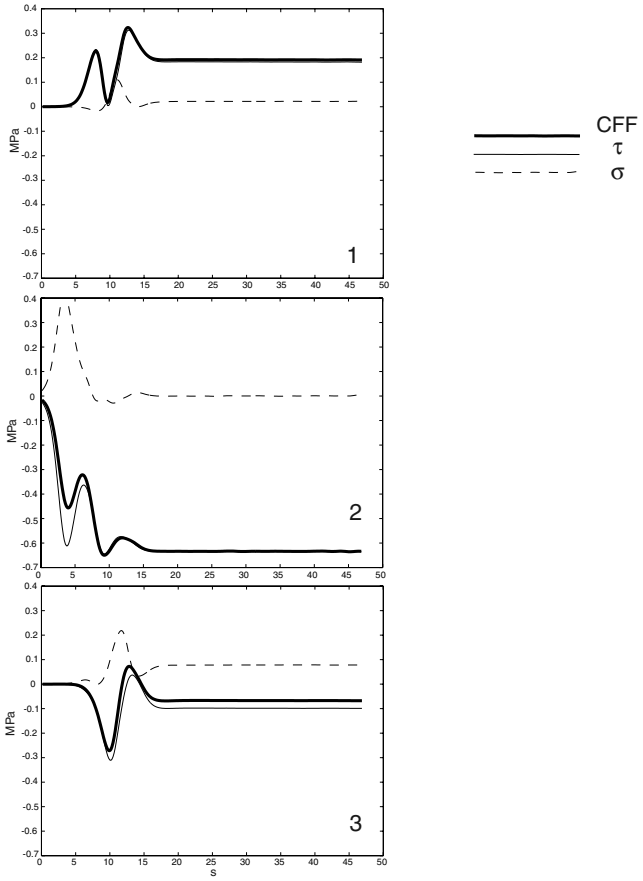

Figure 7. (*Continued*.)

than the complexity of the rupture history, at least for the frequency range investigated in this study and for smooth source time functions considered here.

DYNAMIC STRESS CHANGES FOR AN UNDRAINED ISOTROPIC PORO-ELASTIC MODEL

The Coulomb stress changes discussed in the previous sections have been calculated using the constant apparent friction model defined in eq. (3). Here we aim to compare the time histories of dynamic stress changes calculated with this friction model with an alternative poro-elastic model, named by Beeler *et al.* (2000) and Cocco & Rice (2002), the isotropic poro-elastic model. This model assumes that the pore pressure change is expressed by the mean stress or volumetric stress change

$$\Delta P(\mathbf{y}, t) = -B\,\frac{\Delta\sigma_{kk}(\mathbf{y}, t)}{3}, \tag{4}$$

where B is the Skempton parameter. Therefore, according to the definition of Coulomb stress changes (eq. 1), we have

$$\Delta\mathrm{CFF}(\mathbf{y}, t) = \Delta\tau(\mathbf{y}, t) + \mu\left[\Delta\sigma_n(\mathbf{y}, t) - B\,\frac{\Delta\sigma_{kk}(\mathbf{y}, t)}{3}\right] \tag{5}$$

(for further details see Beeler *et al.* 2000; Cocco & Rice 2002). Eqs (3) and (5) differ only in the model adopted to express the induced pore pressure changes (see eqs 2 and 4). Although eq. (4) is named the isotropic poroelastic model by Cocco & Rice (2002), it should be noted that no poroelastic effects are included in our calculations. We have calculated the dynamic stress changes caused by a normal fault (the 1980 Irpinia event used above) and a strike-slip fault (the model depicted in Fig. 6 and used above). We use a stratified half-space (Table 1) and a Bouchon ramp function with a rise time of 1.4 s and a Haskell-like rupture. We adopted a B value of 0.6. Fig. 12 shows the results of these calculations for the two receivers indicated in the maps included in each panel; for each receiver we plot the transient stress perturbations at two different depths (1 and 5 km). Fig. 12(a) shows the time histories of stress changes caused by the 1980 Irpinia normal faulting earthquake for the two different poroelastic models. Fig. 12(b) shows the same calculations for the strike-slip event of Fig. 6.

The adopted poro-elastic model affects the static stress amplitudes mainly in receiver 2 of Fig. 12(a). The effect on the dynamic (transient) stress changes is less pronounced. The duration of the transient stage and the timing of most of the peaks of dynamic stress are not noticeably affected by the poroelastic model. The differences also depend on the depth of the receiver. For particular receivers (see point 2 at 5 km depth in Fig. 12a) the two poro-elastic models can generate dynamic stress peaks with opposite sign. The differences between the stress time histories calculated with the two distinct poro-elastic models at different depths suggest that the expression adopted to account for pore pressure changes can affect the depth dependence of Coulomb stress changes. These results agree with those discussed by Beeler *et al.* (2000). We point out again that our simulations suggest that the static and the dynamic stress amplitudes depend on the adopted poro-elastic model, at least for particular receiver locations.

DISCUSSION AND CONCLUDING REMARKS

The results presented in this study clearly show that the adopted crustal model, the source time function and the slip duration affect the time histories of coseismic stress perturbations. They influence both the peak amplitudes of dynamic stress changes and the static stress level but, more importantly, they alter the frequency content of transient stress changes. One of the most important results emerging from this investigation is that, within the frequency band investigated in this study ($f < 3$ HZ), the rupture directivity affects the simulated stress time-series more than the details of rupture history and the variations in rupture velocity. The effect of slip duration, represented in our calculations by the rise time, is quite evident: the adopted value of rise time controls the frequency content and the amplitudes of the time history of coseismic stress changes. The rise time effect is more relevant than the details of rupture propagation on the fault plane. Our simulations show that short slip duration and rupture directivity produce evident amplifications of the coseismic stress changes.

These results confirm the findings of Kilb *et al.* (2000, 2002) and Gomberg *et al.* (2000), who proposed that dynamic stress perturbations caused by the Landers earthquake are controlled by rupture directivity, which yields a better correlation between the spatial pattern of Coulomb stress and the seismicity rate changes. According to our results, at high frequencies the dynamic stress perturbations can be even more heterogeneous in time and space than static stress perturbations. However, in this case the transient stress perturbation applied to a single receiver persists for a very short time. Belardinelli *et al.* (2003) concluded that a short persistence reduces the capability of dynamic stress change to trigger earthquakes, unless the

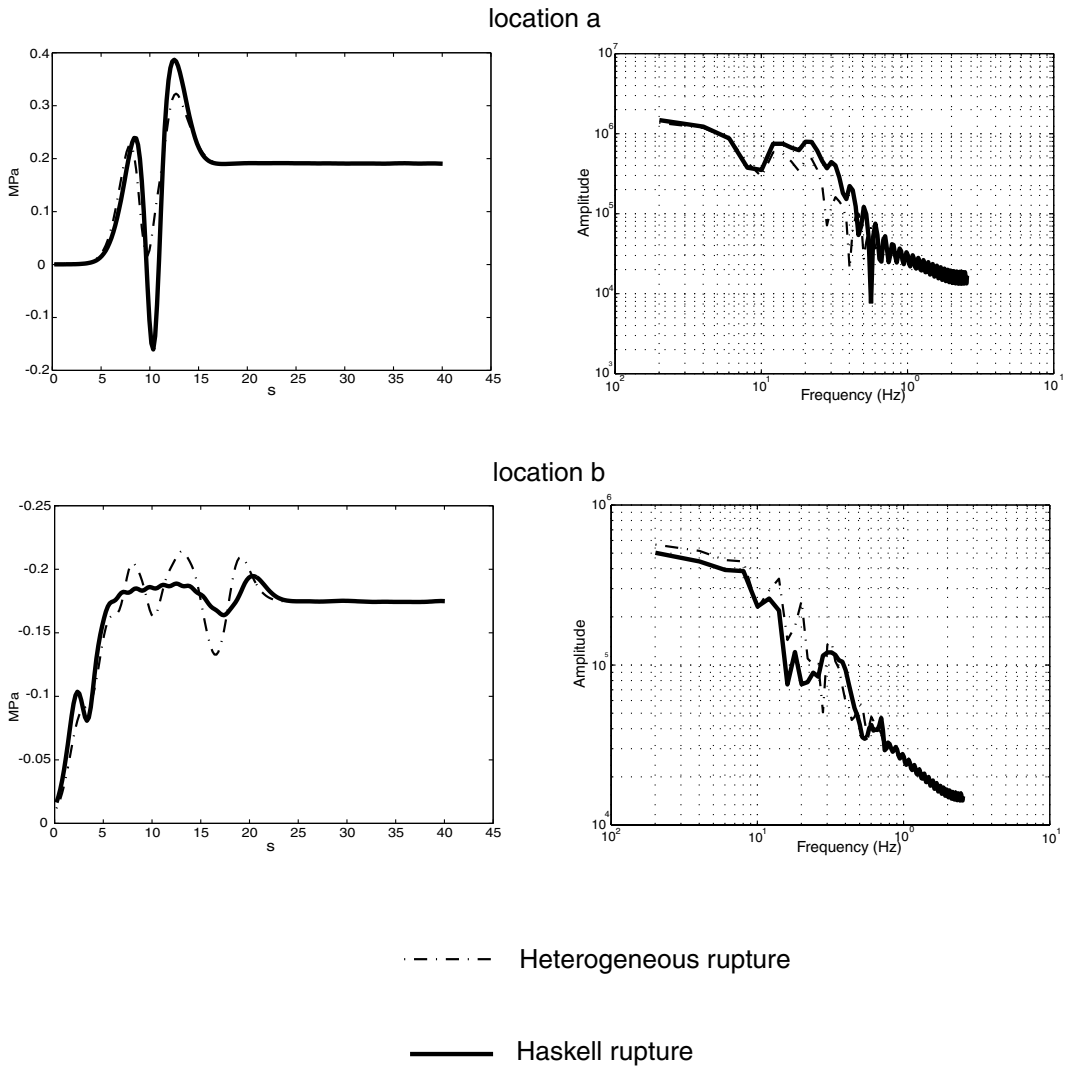

Figure 8. Comparison of the time-series and the Fourier spectra of stress time histories calculated at the two receivers located in opposite positions with respect to the rupture front propagation direction (solid dots in Fig. 6). The other parameters are the same as those adopted in Fig. 7.

transient stress amplitudes are large enough to overcome the frictional resistance.

In this study we have also investigated the attenuation of Coulomb stress amplitudes with distance for different rise time values (see Fig. 5) and different source-to-receiver configurations (see Fig. 11). Dynamic stress amplitudes are less attenuated with distance from the causative faults than static stress changes, in agreement with Cotton & Coutant (1997), but this difference depends on the assumed rise time value (as clearly shown in Fig. 5). Moreover, the rupture directivity produces relative amplifications, but it does not modify the attenuation law. This study also highlights the effects of crustal heterogeneity on the simulated stress time histories. The effect of the crustal model influences both the transient and the static stress perturbations. When the heterogeneous crustal structure is taken into account, the spatial pattern of coseismic stress changes depends strongly on the crustal structure. This should be taken into account in fault interaction studies, which usually show maps of Coulomb stress changes at mid-depth of the seismogenic layer.

In this study, we have also investigated the consequences of the adopted poro-elastic models on the simulated stress time histories. Beeler *et al.* (2000) and Cocco & Rice (2002) have discussed this for static stress changes. We have performed a similar comparison between dynamic stress perturbations. Our results confirm the conclusions of previous studies for static stress changes and show that using different poroelastic models has a smaller effect on dynamic stresses than for static stress.

All the results presented in this study have an important implication: they point out the difficulties in constraining the amplitude of coseismic stress changes caused by an earthquake rupture. Our modelling procedure can only infer a low-frequency image for the coseismic stress pattern, which includes transient and permanent perturbations. The spatial pattern of Coulomb stress change should be calculated taking into account the effect of crustal heterogeneity, rupture directivity and slip duration. We speculate that the lack of knowledge of the source time function to represent slip or slip velocity in kinematic earthquake models is another factor contributing to the limitation in modelling dynamic stress changes.

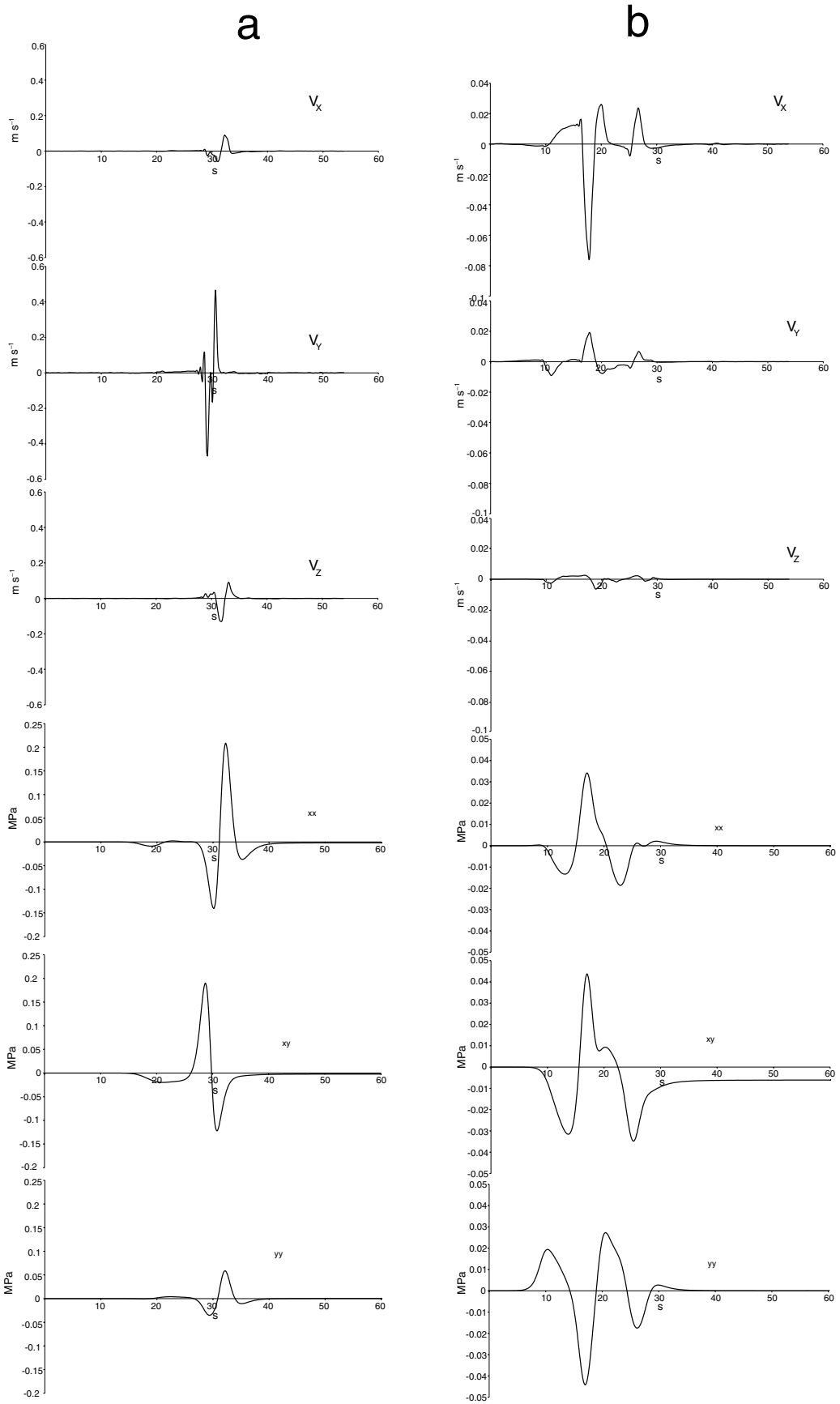

Figure 9. Waveforms of synthetic ground velocity and components of the dynamic stresses as a function of time at the Earth's surface. The locations of receivers a and b are shown by the dark dots in Fig. 6. The rupture model and fault parameters are the same as those adopted in Fig. 6.

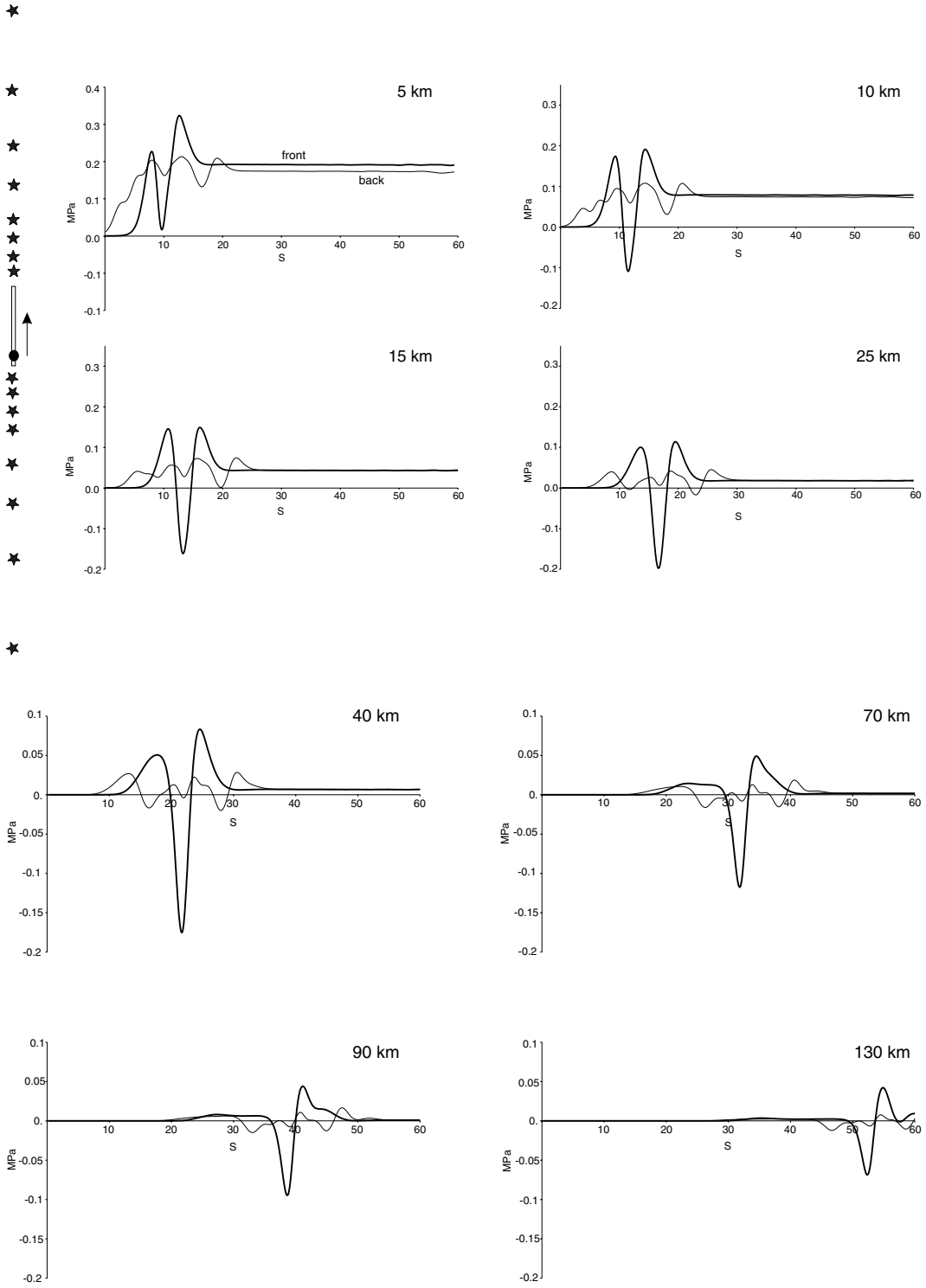

Figure 10. CFF evolution computed at receivers distributed along the strike direction at a depth of 7 km. The receiver points are symmetrically placed with respect to the fault plane along the fault strike, as shown in the inset sketch. The distance from the nearest edge of the fault is indicated. The thick and thin lines are the CFFs in and opposite to the directions of rupture propagation, respectively. The near field is displayed in (a) and the far field in (b). The fault parameters are the same as those adopted in Fig. 6.

ACKNOWLEDGMENTS

We wish to thank Maurizio Bonafede, Andrea Bizzarri, Sandy Steacy, Concetta Nostro and Davide Piccinini for helpful discussions. Special thanks go to Joan Gomberg, Michel Bouchon and Torsten Dahm for reviewing this paper. We are indebted to Olivier Coutant and Fabrice Cotton for the collaborations and the availability of their code. This study has been partially

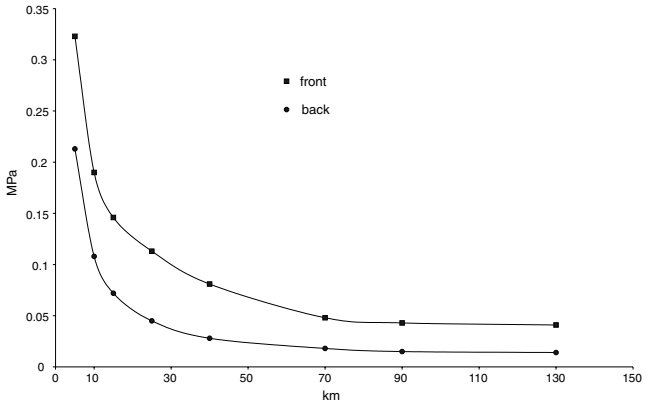

Figure 11. Attenuation of the dynamic and static amplitude of the CFF along the two opposite receiver arrays. The *x*-axis is the distance of the receiver from the nearest fault edge. Squares refer to the highest dynamic stress value in the rupture direction, while the circles refer to the value in the direction opposite to the rupture motion. The fault parameters are the same as those adopted in Fig. 6.

supported by the EC grant ENC-CT1-199900001 (contract PRESAP).

REFERENCES

Antonioli, A., Cocco, M., Das, S. & Henry, C., 2002. Dynamic stress triggering during the great 25 March 1998 Antartic plate earthquake, *Bull. seism. Soc. Am.,* **92,** 896–903.

Beeler, N.M., Simpson, R.W., Hickman, S.H. & Lockner, D.A., 2000. Pore fluid pressure, apparent friction, and Coulomb failure, *J. geophys. Res.,* **105,** 25 533–25 542.

Belardinelli, M.E., Cocco, M., Coutant, O. & Cotton, F., 1999. Redistribution of dynamic stress during coseismic rupture: evidence for fault interaction and earthquake triggering, *J. geophys. Res.,* **104,** 14 925–14 945.

Belardinelli, M.E., Bizzarri, A., Cocco, M., 2003. Earthquake triggering by static and dynamic stress changes, *J. geophys. Res.,* **108,** B3, 2135, doi:10.1029/2002JB001779, 2003.

Bouchon, M., 1981. A simple method to calculate Green's function for layered media, *Bull. seism. Soc. Am.,* **71,** 959–971.

Cocco, M. & Pacor, F., 1993. The rupture process of the 1980 Irpinia, Italy, earthquake from the inversion of strong motion waveforms, *Tectonophysics,* **218,** 157–177.

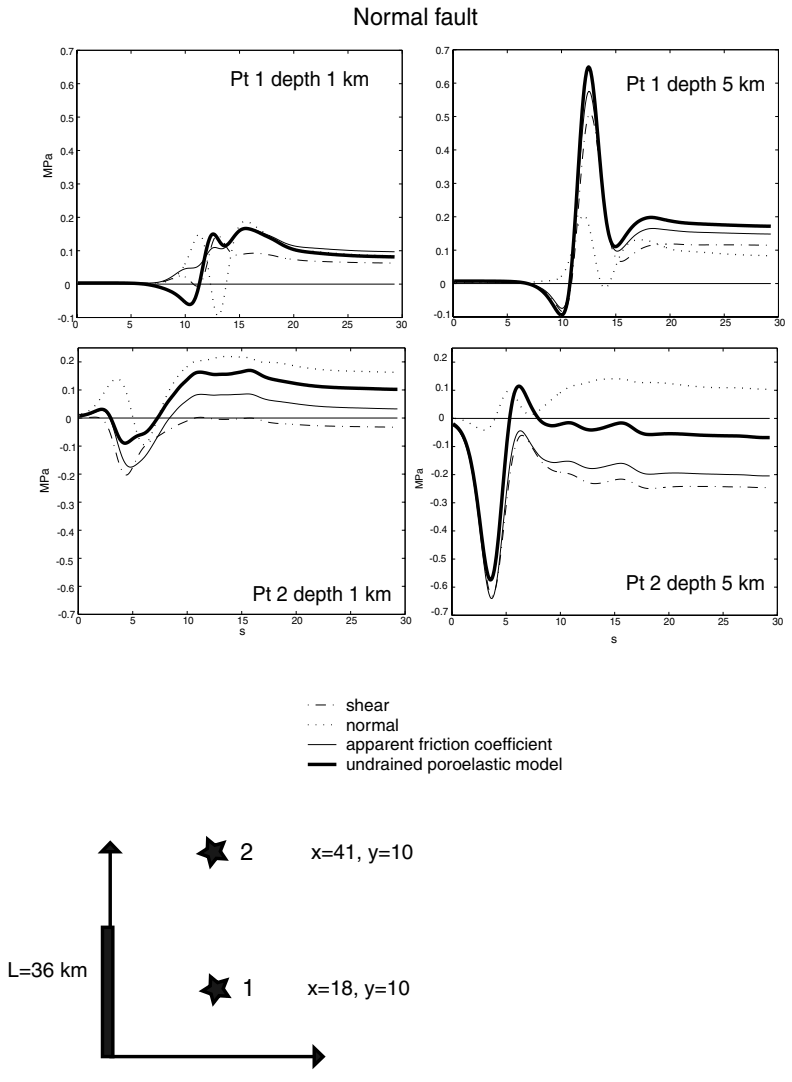

Figure 12. Coulomb failure function computed with the two approximated different formulation presented in the text (eqs 3 and 5). In (a) we represent the normal fault case and in (b) the transform fault case. The positions of the receiver are indicated by the black stars and the stress is evaluated at two different depths, 1 and 5 km. The dotted line and the dot-dashed line show the normal and shear stress, respectively. The thin solid line refers to the apparent friction formulation (eq. 3), while the thick solid line refers to the isotropic poroelastic model expression of the CFF (eq. 5).

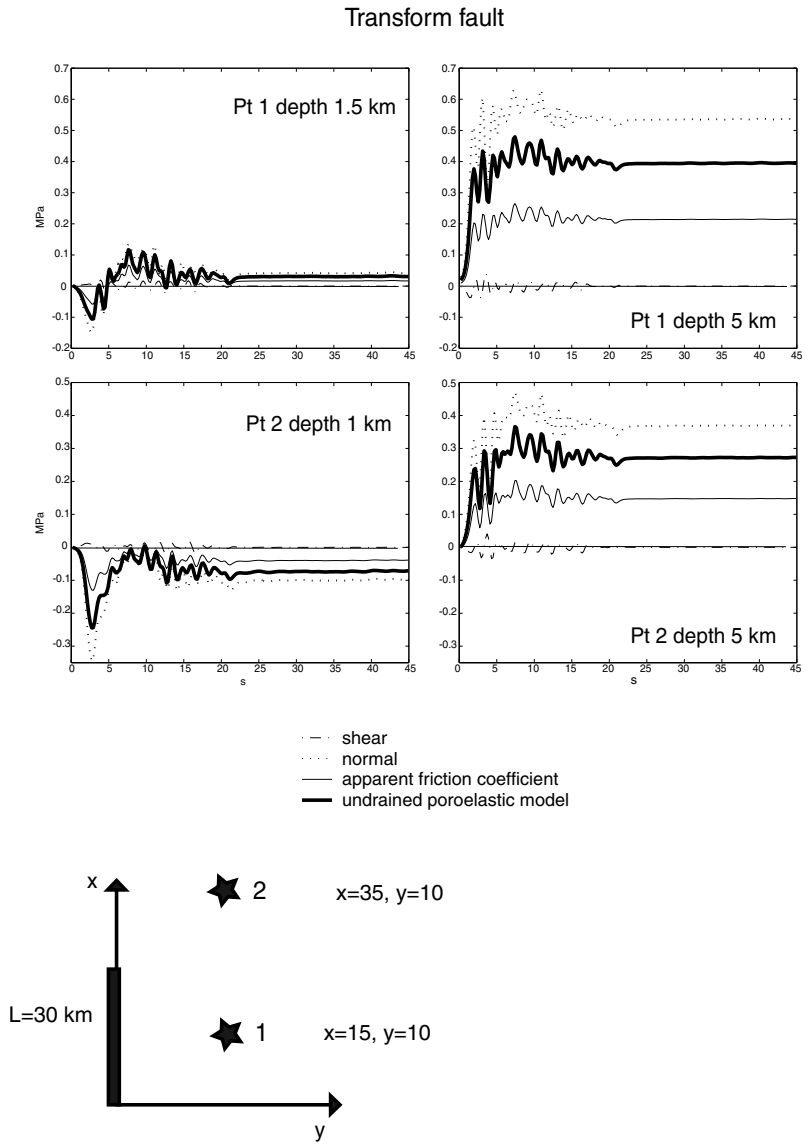

Figure 12. (*Continued*.)

Cocco, M. & Rice, J.R., 2002. Pore pressure and poroelasticty effects in Coulomb stress analysis of earthquake interaction, *J. geophys. Res.,* **107,** 10, ESE 2, Feb.

Cotton, F. & Coutant, O., 1997. Dynamic stress variations due to shear faulting in a plane layered medium, *Geophys. J. Int.,* **128,** 676–688.

Giardini, D., 1993. Teleseismic observation of the November 23, 1980, Irpinia earthquake, *Ann. Geofis.,* **36,** 17–25.

Gomberg, J., 2001. The failure of earthquake failure models, *J. geophys. Res.,* **106,** 16 253–16 263.

Gomberg, J., Beeler, N.M., Blanpied, M.L. & Bodin, P., 1998. Earthquake triggering by transient and static deformation, *J. geophys. Res.,* **103,** 24 411–24 426.

Gomberg, J., Beeler, N. & Blanpied, M., 2000. On rate-state and Coulomb failure models, *J. geophys. Res.,* **105,** 7857–7871.

Gomberg, J., Bodin, P. & Reasemberg, P., 2003. Observing earthquakes triggered in the near field by dynamic deformations, *Bull. seism. Soc. Am.,* **93,** 118–138.

Harris, R., 1998. Introduction to special section: stress triggers, stress shadows, and implications for seismic hazard, *J. geophys. Res.,* **103,** 24 347–24 358.

Harris, R.A. & Simpson, R.W., 1992. Changes in static stress on southern California faults after the 1992 Landers earthquake, *Nature,* **360,** 251–254.

Kennet, B.L. & Kerry, N.J., 1979. Seismic wave in a stratified half space, *J. R. Astron. Soc.,* **84,** 557–583.

Kilb, D., Gomberg, J. & Bodin, P., 2000. Triggering of earthquake aftershocks by dynamic stresses, *Nature,* **408,** 570–574.

Kilb, D., Gomberg, J. & Bodin, P., 2002. Aftershock triggering by complete Coulomb stress changes, *J. geophys. Res.,* **107**, ESE 2, Apr.

King, G.C.P. & Cocco, M., 2000. Fault interaction by elastic stress changes: new clues from earthquake sequences, *Adv. Geophys.,* **44,** 1–38.

King, G.C.P., Stein, R.S. & Lin, J., 1994. Static stress changes and the triggering of earthquakes, *Bull. seism. Soc. Am.,* **84,** 935–953.

Nostro, C., Cocco, M. & Belardinelli, M.E., 1997. Static stress changes in extensional regimes: an application to southern Appennines (Italy), *Bull. seism. Soc. Am.,* **87,** 234–248.

Okada, Y., 1985. Surface deformation due to shear and tensile faults in a half-space, *Bull. seism. Soc. Am.,* **75,** 1135–1154.

Okada, Y., 1992. Internal deformation due to shear and tensile faults in a half-space, *Bull. seism. Soc. Am.,* **82,** 1018–1040.

Pantosti, D. & Valensise, G., 1990. Faulting mechanism and complexity of the 23 November, 1980, Campania-Lucania earthquake inferred from surface observations, *J. geophys. Res.,* **95,** 15 319–15 341.

Rice, J.R. & Cleary, M.P., 1976. Some basic stress diffusion solutions for fluid saturated elastic porous media with compressible constituents, *Rev. Geophys.,* **14,** 227–241.

Scholz, C.H., 1998. Earthquakes and friction laws, *Nature,* **391,** 37–42.

Spudich, P. & Frazer, L.N., 1984. Use of ray theory to calculate high-frequency radiation from earthquake sources having spatially variable rupture velocity and stress drop, *Bull. seism. Soc. Am.,* **74,** 2061–2082.

Stein, R.S., 1999. The role of stress transfer in earthquake occurrence, *Nature,* **402,** 605–609.